

Transition due to isolated roughness in a swept wing boundary layer

Zoppini, Giulia; Ragni, Daniele; Kotsonis, Marios

DOI

[10.1063/5.0101187](https://doi.org/10.1063/5.0101187)

Publication date

2022

Document Version

Final published version

Published in

Physics of Fluids

Citation (APA)

Zoppini, G., Ragni, D., & Kotsonis, M. (2022). Transition due to isolated roughness in a swept wing boundary layer. *Physics of Fluids*, 34(8), Article 084113. <https://doi.org/10.1063/5.0101187>

Important note

To cite this publication, please use the final published version (if applicable).
Please check the document version above.

Copyright

Other than for strictly personal use, it is not permitted to download, forward or distribute the text or part of it, without the consent of the author(s) and/or copyright holder(s), unless the work is under an open content license such as Creative Commons.

Takedown policy

Please contact us and provide details if you believe this document breaches copyrights.
We will remove access to the work immediately and investigate your claim.

Transition due to isolated roughness in a swept wing boundary layer

Cite as: Phys. Fluids **34**, 084113 (2022); <https://doi.org/10.1063/5.0101187>

Submitted: 30 May 2022 • Accepted: 26 July 2022 • Accepted Manuscript Online: 26 July 2022 •
Published Online: 25 August 2022

Published open access through an agreement with Technische Universiteit Delft Faculteit Luchtvaart- en Ruimtevaarttechniek

 Giulia Zoppini,  Daniele Ragni and  Marios Kotsonis



View Online



Export Citation



CrossMark

ARTICLES YOU MAY BE INTERESTED IN

[An experimental modal testing method for subcritical flow around a cylinder](#)

Physics of Fluids **34**, 083608 (2022); <https://doi.org/10.1063/5.0101624>

[Mechanism of hysteresis and uncontrolled deflection in jet vectoring control based on Coanda effect](#)

Physics of Fluids **34**, 084107 (2022); <https://doi.org/10.1063/5.0101994>

[Sidewall effect on turbulent band in subcritical transition of high-aspect-ratio duct flow](#)

Physics of Fluids **34**, 084112 (2022); <https://doi.org/10.1063/5.0096626>

Physics of Fluids

Submit Today!

Special Topic: Hydrogen Flame and Detonation Physics



Transition due to isolated roughness in a swept wing boundary layer

Cite as: Phys. Fluids **34**, 084113 (2022); doi: 10.1063/5.0101187

Submitted: 30 May 2022 · Accepted: 26 July 2022 ·

Published Online: 25 August 2022



View Online



Export Citation



CrossMark

Giulia Zoppini,^{1,a)}  Daniele Ragni,²  and Marios Kotsonis¹ 

AFFILIATIONS

¹Section of Aerodynamics, Delft University of Technology, Delft 2629HS, The Netherlands

²Section of Wind Energy, Delft University of Technology, Delft 2629HS, The Netherlands

^{a)}Author to whom correspondence should be addressed: g.zoppini@tudelft.nl

ABSTRACT

The present work is dedicated to the investigation of the effect of an isolated roughness element on a swept wing boundary layer. In particular, the flow modifications incurred by a single cylindrical element applied on a swept wing model are measured, toward describing the nature of the perturbations introduced in the flow field, their development in the near and far wake region, as well as their eventual breakdown. The measurements are performed using infrared thermography, to achieve a general overview of the element wake origin and spatial spreading. Local quantitative characterization of the stationary and unsteady disturbances evolving in the flow is instead acquired through hot wire anemometry. When present in an undisturbed laminar boundary layer, isolated roughness elements are found to introduce flow disturbances, which lead to the formation of a turbulent wedge. As it develops downstream, the wedge undergoes rapid spanwise expansion, affecting the adjacent laminar flow regions. The wedge origin and development is mostly associated with the instabilities introduced by the shedding process initiated in the roughness element wake, comparably to the dominant flow features characterizing the transition of two-dimensional boundary layers conditioned by an isolated roughness element. Nonetheless, the presence of the crossflow velocity component in the boundary layer baseflow notably affects the overall flow development, introducing an asymmetric evolution of the main flow features.

© 2022 Author(s). All article content, except where otherwise noted, is licensed under a Creative Commons Attribution (CC BY) license (<http://creativecommons.org/licenses/by/4.0/>). <https://doi.org/10.1063/5.0101187>

I. INTRODUCTION

The importance of surface roughness in the laminar-to-turbulent transition process of boundary layers (BL) is well established. In particular, for both two-dimensional (2D) and three-dimensional (3D) boundary layers, a large isolated 3D roughness element applied on the wing surface can drive the transitional process via the initiation and spreading of a turbulent wedge.^{3,19,21,35} Already from these early studies, the geometry and dimensions of the roughness elements are found to play a crucial role in the onset and development of flow instabilities in the element wake and ensuing transition. As such, numerous works^{21,39} focused on determining whether a given roughness geometry would give rise to turbulent flow, resulting in the definition of the roughness Reynolds number as a predicting parameter ($Re_k = \frac{k|\mathbf{u}(k)|}{\nu}$ with $|\mathbf{u}(k)|$ boundary layer velocity at the element height k and ν kinematic viscosity). In particular, the Re_k proved to be a useful indicator for the distinction between roughness configurations of super-critical or critical nature, which, respectively, induce flow tripping in the element vicinity or introduce instabilities that develop and amplify downstream, leading to laminar breakdown and turbulence onset. However,

this geometrical parameter does not provide a satisfactory characterization of the flow mechanisms ultimately responsible for the boundary layer transition to turbulence.

The flow topology aft of isolated roughness elements has been widely investigated, starting from flow visualizations dedicated to the analysis of turbulent wedges formation and downstream evolution in 2D boundary layers.^{3,19,35} In particular, experimental and numerical investigations^{3,8,26,28} observed that as the incoming laminar BL encounters the roughness element, upstream of the element the spanwise vorticity rolls up, inducing the formation of a horseshoe vortex (HSV) system. The two steady counter-rotating HSV legs wrap around the element and extend downstream, driving the re-orientation of vorticity in the streamwise direction and initiating a momentum redistribution process. This effect can be traced to the lift-up mechanism,²⁵ namely, the deflection of low-speed flow toward the upper regions of the boundary layer and vice versa, leading to the formation of high-speed streaks on the outer side of the HSV legs. More downstream, the structure evolution along with the momentum redistribution they induce initiates a cascading configuration of low- and high-speed

streaks destabilizing the wedge edges, enhancing its spreading and the onset of turbulence (e.g., Refs. 5, 13, and 22).

Hot-wire anemometry measurements³ performed on the HSV legs, identified velocity fluctuations occurring with frequency peaks corresponding to unsteady shedding from the roughness element. Additionally, the onset of turbulent flow is found to occur at a finite chordwise distance from the roughness element location, even for high Re_k geometries.²¹ These observations suggest that the transitional process induced by isolated elements is most likely initiated by an instability developing in the reversed flow region within the element wake. Further investigations^{1,21} proved that the roughness initiates a process of hairpin vortex shedding from the separated region on the element's upper surface. These results highlight the presence of a periodic shedding process corresponding to a range of Strouhal numbers (based on the element height, the local flow velocity, and the shedding frequency) of $St = 0.05\text{--}0.4$, with a monotonic increase in the intensity of primary fluctuations (and their harmonics) for increasing Re_k (up to $Re_k = 1000$). Recent DNS investigations^{8,13,26} and experiments^{4,16,22,28,45} further confirmed these observations. Specifically, these studies indicated that transition induced by isolated roughness elements occurs due to high-frequency instabilities of Kelvin–Helmholtz type, shed by the high shear regions forming in the perimeter (i.e., top and sides) of the roughness element wake. Recent works combining experimental and numerical stability analysis^{8,9,12,17,18,28,29} showed that the observed instabilities can either result from the amplification of a range of instability modes in the element wake, or from the strong enhancement of a specific mode, possibly introduced by external forcing. Accordingly, the roughness element can, respectively, behave as an amplifier in the first case, exciting a range of non-orthogonal frequencies,^{8,12,40,44} or as a resonator, only enhancing a precise unstable frequency.^{9,28} The occurring scenario depends on multiple parameters, in which Re_k , the aspect ratio of the protuberance k/D (with D being the element diameter), the shear ratio k/δ^* (with δ^* being the local BL displacement thickness), and the freestream turbulence intensity play a major role. Furthermore, the near-wake velocity deficit is observed to evolve into a far-wake accelerated region surrounded by low-speed flow.^{20,26} Depending on the roughness geometry and BL scales, this process can either enhance the instabilities initiating the turbulent wedge or result into perturbation decay, thus stabilizing the boundary layer. The latter scenario has given space to numerous transient growth and flow stability investigations (e.g., Refs. 11, 12, 16, 26, and 43).

Despite the numerous investigations dedicated to isolated roughness element effects in 2D boundary layers, considerably fewer recent works directly investigate such effects in 3D boundary layers (e.g., Refs. 6, 34, and 38). Most of the available works have been dedicated to the analysis of the mechanisms dominating the wedge origin and downstream development,³⁰ as the low- and high-speed streaks cascade driving the spanwise expansion of the wedge edges.^{5,22} By measuring the BL evolution aft of the isolated element, previous works³⁰ identified a single low-speed streak developing downstream of the element, evolving with an inclination with respect to the freestream flow typically pertaining to the evolution of crossflow vortices. However, it must be noted that the Re_k range covered by the aforementioned study³⁰ was limited to highly sub-critical regimes, thus not representative of near-tripping behavior. Similar results were obtained from DNS investigations,^{7,24,41} which identified the wall-normal and spanwise shear layers developing in the immediate vicinity of the element as

responsible for initiating the instabilities dominating the transitional process. This observation suggests the near-element flow topology and the instability origin for isolated elements in 2D and 3D boundary layers are strongly comparable.²⁴ Accordingly, we provided that they are not triggered upstream by other roughness features, and the modal crossflow instabilities that usually dominate the transitional scenario of smooth swept wings (e.g., Refs. 6, 30, and 34) appear to have little effect on the development of the near-element flow and on the instabilities initiated by the isolated roughness element. This behavior can be related to the amplitude of the applied isolated roughness element, which is sufficiently large to operate in a critical regime close to flow tripping, as will be further outlined in the remainder of this work. Nonetheless, the aforementioned DNS investigations observe a significant asymmetry in the flow features pertaining to the wake evolution, which can be related to the existence of a crossflow velocity component in the BL. Specifically, for any streamwise-oriented vortical structure, the crossflow direction of rotation is favored, thus developing a flow field dominated by co-rotating vortices. This behavior leads to significant differences between the downstream flow evolution in 2D and 3D boundary layers, mainly due to the loss of symmetry.¹⁰

Within the framework established by the aforementioned investigations, a notable lack of experimental measurements detailing the effect of isolated roughness elements is swept wing boundary layers, which is identified. This is particularly evident for near-critical regimes ($Re_k \approx 200$), which are representative of large real-life roughness features such as rivets or debris. The present work experimentally describes the isolated element near-wake flow field in a 3D boundary layer, to identify the flow features dominating the flow development and characterize the nature of the induced instability. The chosen amplitude for the roughness element is intentionally set to near-critical levels, thus ensuring a strong boundary layer forcing, effectively bypassing classical modal crossflow instabilities inherent to micron-sized roughness elements. Nonetheless, as will be shown, the presence of the crossflow velocity component in the boundary layer baseflow affects the overall downstream flow development, introducing an asymmetric evolution of the identified flow features. Consequently, the withstanding relation between the rapid near-element instability onset and the 3D boundary layer transition in the near-critical amplitude regime is analyzed. This investigation allows for the identification of similarities and discrepancies between the considered 3D boundary layer scenario and the well-known 2D transitional scenario. For the experimental campaign, a single cylindrical element is placed in the undisturbed laminar boundary layer developing on the swept wing surface, and measurements are taken at three Re numbers by varying the freestream velocity. This grants the possibility of studying the flow behavior in the presence of a super-critical or a critical forcing configuration without changing the geometrical characteristics of the roughness element. Infrared thermography imaging is employed to investigate the base flow topology, including a quantification of the onset location and chordwise development of the developing turbulent wedge. Additionally, local hot-wire anemometry scans are performed, allowing for detailed characterization of the flow features dominating the element near-wake, as well as of the development of stationary and unsteady structures. In particular, the time-dependent velocity signal is analyzed to investigate the velocity fluctuations spectral characteristics, which provide fundamental information regarding the nature and evolution of the developing instabilities.

TABLE I. Geometric parameters of the M3J swept wing model.³⁷ Wing sweep angle (Λ), wing aspect ratio (AR), wing span along Z (b), wing chord along x (c_x), wing chord along x (c), wing surface (S), and background wing surface roughness (R_q).

Parameter	Λ	AR	b	c_x	c	S	R_q
Value	45°	1.01	1.25 m	1.27 m	0.9 m	1.58 m ²	0.20 μ m

II. METHODOLOGY

A. Wing model and wind tunnel facility

The presented measurements are performed on an in-house designed, constant-chord swept wing model (M3J),³⁷ with main geometrical parameters given in Table I. The wing is purposely designed and widely exploited to investigate the physics of primary and secondary CFI that dominate the boundary layer development and transition in these conditions.

The measurements are performed in the low turbulence wind tunnel (LTT), an atmospheric low-speed closed return tunnel at the TU Delft developing low levels of freestream turbulence in the test section flow.³⁶ In the present work, measurements are performed on the pressure side of the wing at three freestream Reynolds numbers, namely, $Re_{c_x} = 1.45 \times 10^6$, 1.35×10^6 , 1.27×10^6 , while the angle of attack is kept fixed at $\alpha = -3.36^\circ$. Furthermore, to inform the scaling of the problem, a numerical boundary layer solution is computed for each of the three tested Re_{c_x} based on the experimentally measured pressure gradient, as per the procedure described by Serpieri.³⁶

Throughout this work, two coordinate reference systems are used: one is integral with the wind tunnel floor, with spatial components X, Y, and Z and velocity components U, V, and W; the second one with z axis aligned to the leading edge with spatial components x, y, and z and velocity u, v, and w. A sketch of the swept wing and related coordinate reference systems is reported in Fig. 1(a).

B. Isolated roughness element

As previously stated, the present study aims at investigating the effect of an isolated roughness element on the swept wing boundary layer development and transition. The selection of the roughness element geometry follows from past experimental investigations.^{27,38} An isolated cylindrical element with height $k = 0.5$ mm and nominal diameter $D = 6$ mm is positioned at $x_r/c = 0.15$ through a layer of

TABLE II. Geometric parameters of the measured roughness configurations.

Parameter	x_r/c	k (mm)	D (mm)	D/k	Re_{c_x}	Re_k	k/δ^*
Value	0.15	0.5	6	12	1.45×10^6	251	0.90
	0.15	0.5	6	12	1.35×10^6	219	0.85
	0.15	0.5	6	12	1.27×10^6	198	0.83

double-sided tape (nominal thickness, 0.01 mm). The roughness element and its location on the wing surface are sketched in Fig. 1. The element is machined from copper rods having the same D, then polishing the upper and lower circular surfaces to remove imperfections.²⁷

The element geometry can be related to the BL evolution through the roughness Reynolds number.^{19,24,30,32} This geometrical parameter is defined as $Re_k = \frac{k \times |u(k)|}{\nu}$ and is widely applied as a preliminary estimate of the effectiveness of a given element in influencing BL transition. In fact, the Re_k value can be correlated with its critical value (i.e., the lower value of Re_k corresponding to a super-critical roughness configuration) to predict the boundary layer transitional behavior aft of the roughness element. The critical value of Re_k scales with $(k/D)^{2/5}$, starting from values in the range $Re_{k,crit} = 600-900$ for an element with $k/D = 1$.^{16,21} Based on the element k/D ratio, the $Re_{k,crit}$ value for the present application ranges between 225 and 335. Consequently, the three values of Re_{c_x} considered throughout this investigation, corresponding to $Re_{k_1} = 251$, $Re_{k_2} = 219$, and $Re_{k_3} = 198$ for decreasing Re_{c_x} , span super-critical, and critical transitional behavior (Table II).

In addition to the roughness Reynolds number, a second geometrical parameter can potentially be used to orient the different regimes governing instability growth and breakdown in the considered cases. This parameter has been found to successfully describe cases in 2D boundary layers, identifying the type of instability developing in the wake of a cylindrical roughness.⁸ In particular, the shear ratio k/δ^* with δ^* being the local boundary layer displacement thickness δ^* at x_r/c , is considered to be representative of the characteristic magnitude of the shear of the laminar BL flow impinging on the roughness element. For the roughness configurations considered throughout this work, the k/δ^* is estimated to be 0.9, 0.85, and 0.83 for decreasing Re_k (Table II). These values all fall underneath the k/δ^* range at which varicose modes are found to dominate the boundary layer evolution aft of the roughness element in 2D cases (i.e., $k/\delta^* \simeq 1.5-2$).⁸ Nonetheless, it

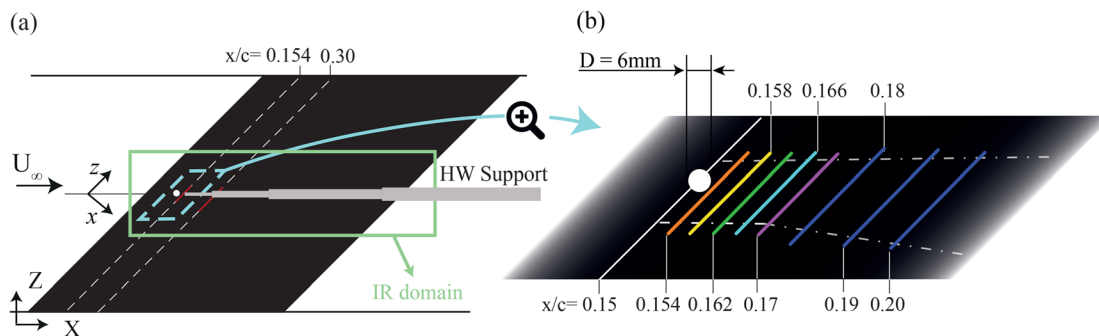


FIG. 1. (a) Sketch of experimental setup and coordinate reference systems (not to scale). Y axis and y axis are directed toward the reader. IR domain (green rectangle); HW most upstream and downstream plane (red line). (b) Zoomed-in sketch of hot-wire acquisition planes in the element vicinity [dashed blue region in (a)].

must be noted here that the aforementioned critical parameters are widely established for isolated elements in 2D boundary layers. Their applicability in 3D boundary layers, such as the one considered in the present work, is not equally established, and they are taken here only as preliminary estimates of the governing dynamics.

C. Measurement techniques and data analysis

Throughout the present study, both the isolated element near-wake and the far-wake flow features are investigated. Global flow features are monitored through infrared thermography (IR), while local quantitative information is extracted through hot-wire anemometry (HWA) measurements. Hereafter, the setup and methodology pertaining to these measurement techniques are described.

1. Infrared thermography

Infrared thermography^{6,14,36} images the wing surface temperature, which is subject to external heat deposition. The method capitalizes on Reynolds' analogy, namely, regions of low wall shear (i.e., laminar regions), develop a lower convective heat transfer coefficient, thus appearing colder, while regions of high wall shear (i.e., turbulent regions) appear warmer. This provides a global overview of the wedge origin and downstream evolution, indicating the loci of transition.

In the present work, the pressure side of the model is imaged by an Optris PI 640 IR radiometric camera through an opening cut in the vertical sidewall of the test section. Surface temperatures are acquired at the chosen Reynolds numbers for a constant angle of attack $\alpha = -3.36^\circ$. The camera images the model surface from leading edge to trailing edge, acquiring a field of view centered at the wing midspan and spatial resolution of 0.85 mm/px. The acquired IR domain is outlined in green in Fig. 1(a). Snapshots are taken at a frequency of 4 Hz, collecting 80 images at each condition that are then averaged to reduce the signal-to-noise ratio. During the acquisition, to maintain a positive thermal contrast between the laminar-turbulent BL region, the model is externally heated by halogen lamps (2×500 W and 3×400 W).

The collected IR images are geometrically mapped to the wing-attached Cartesian framework (XYZ) through an in-house calibration procedure³³ and further post-processed for enhancing the contrast.

2. Hot-wire anemometry

Hot-wire anemometry (HWA) is employed to collect local and temporal information on the near-element velocity fields, in order to characterize both steady and unsteady perturbations developing in the flow field. HWA measurements are acquired by operating a single-wire Dantec Dynamics 55P15 boundary layer probe through a TSI IFA-300 constant temperature bridge featuring automatic overheat ratio adjustment. An automated traverse system mounted in the wind tunnel diffuser holds the sensor, granting the motion in the three XYZ directions with step resolution of $2.5 \mu\text{m}$ in all axes [sketched in Fig. 1(a)]. Despite the overall stability of the tunnel flow conditions, the flow temperature and pressure are continuously monitored to account for the small changes occurring during the acquisition run, properly correcting the calibrated HWA signal.

The hot-wire acquisitions are performed in the zy plane at different chord locations, mostly concentrated in the element vicinity. An ensemble of HWA scans collected in the spanwise and wall-normal

directions (i.e., in the zy plane) builds up each x/c plane. Every wall-normal velocity profile is measured by acquiring 30 equally spaced point-wise measurements along y . At each point, the CTA bridge signals are sampled for 2 s at a frequency of $f_s \simeq 51.2$ kHz and filtered through an analog low-pass filter (cutoff frequency of 20 kHz) before amplification. To account for the BL growth along the wing chord, the wall-normal spacing of the point-wise measurements is adjusted to capture the whole boundary layer evolution from the near-wall region ($20\% U_\infty$) to the local freestream. Accordingly, for the near-element planes [i.e., $x/c = 0.158, 0.162, 0.166$, and 0.170 , sketched in Fig. 1(b)] the final y -spacing is set to 0.1 mm, while for the more downstream planes (i.e., $x/c = 0.18, 0.19, 0.20, 0.25$, and 0.3), it is changed to 0.15 mm. Once the acquisition of a BL profile is completed, the probe moves to the following spanwise location, repeating the measurement procedure until the set number of BL scans is acquired for the considered zy plane. The infrared image analysis gives an estimation of the expansion and inclination of the developing wedge with respect to the freestream direction. Consequently, the origin and span-wise extent of the HWA acquisition in the zy plane are adjusted at each x/c of interest. Specifically, for the near-element planes, the span-wise spatial resolution is kept constant to 0.5 mm providing a 30 mm spanwise extent; for the downstream chord locations considered, it is doubled in order to accommodate the spreading of the wedge. A Xz HWA plane is also acquired at a fixed wall distance of $y = 1$ mm. In this case, the velocity scans are composed of single point acquisitions collected along the spanwise direction (z) with a spacing of 1 mm. Successive spanwise scans are measured at a chordwise distance (X) of 1.2 mm.

For the entirety of the performed measurements, the hot-wire probe is kept aligned to the Z direction; therefore, at each point, the velocity signal acquired by the sensor is a projection of the instantaneous velocity components, which can be reconstructed as

$$\bar{U}(y, z) = \sqrt{(u \times \cos(45^\circ))^2 + (w \times \sin(45^\circ))^2 + (v)^2}. \quad (1)$$

During data analysis, the measured velocity fields are normalized by the experimentally measured freestream velocity \bar{U}_∞ . The wall-normal distance y and the spanwise coordinate z are instead non-dimensionalized by δ^* computed from the numerical boundary layer solution for Re_{kl} at $x/c = 0.15$ (namely $\bar{\delta}^* = 0.595$ mm).

The time average of the acquired HWA velocity signal $\bar{U}(y, z)$ is computed to investigate the stationary flow features. The spanwise extension of the acquired velocity fields accommodates the flow region corresponding to the instability development at each considered chord location. Additionally, each field also includes a portion of the undisturbed laminar boundary layer developing on both sides of the perturbed flow region. This is visible in Fig. 2(a), where the unperturbed boundary layer flow develops on the left and right, respectively, of the two vertical dash-dotted lines. Therefore, the spanwise average of the velocity signal of the unperturbed flow region at each chord location provides an estimation of the laminar boundary layer baseline development $\bar{U}_b(y)$. Moreover, each of the laminar \bar{U}_b profiles acquired outside of the perturbed flow region allows for the identification of the wall location at the corresponding spanwise coordinate (\bar{z}). In particular, each acquired boundary layer velocity profile $\bar{U}(y, \bar{z})$ is assumed to evolve linearly in the wall vicinity, in agreement with the typical form of the laminar BL velocity profile. Therefore, the BL velocity values can be linearly extrapolated up to the y -location corresponding to

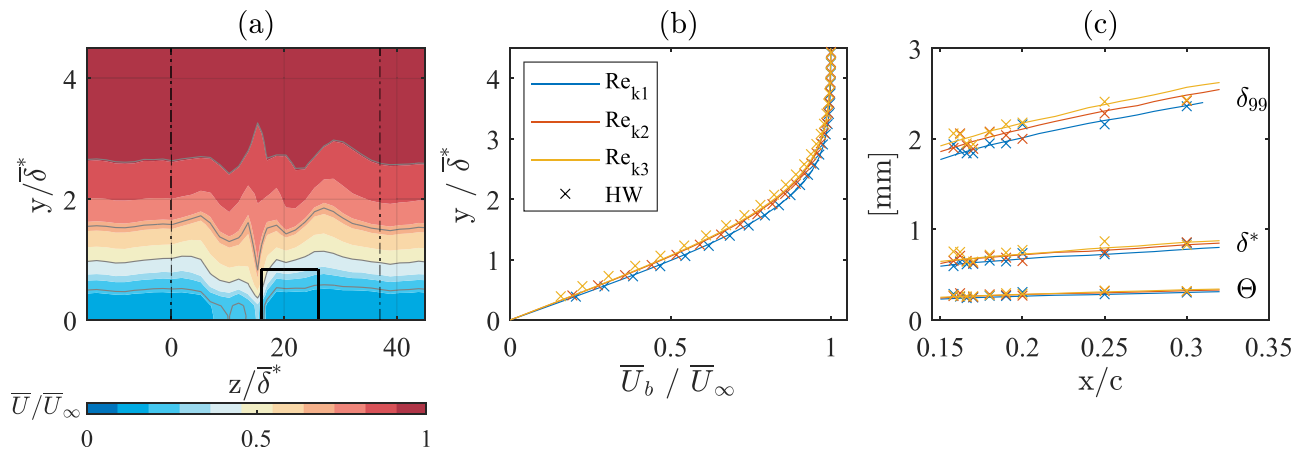


FIG. 2. (a) Time-averaged HWA velocity field for Re_{k_1} at $x/c = 0.2$. Velocity isolines plotted every 20% of \bar{U}_∞ (gray lines); element location (black rectangle); limits of the perturbed flow region (vertical - lines). Comparison between (b) HWA (\times) and numerical (-) BL evolution along y extracted at $x/c = 0.2$; (c) chordwise evolution of BL parameters computed from HWA (\times) and numerical BL profiles (-).

the local $\bar{U}(y, \bar{z}) = 0$. This procedure can be repeated on both sides of the perturbed flow region, such that a linear interpolation along the z direction defines the wall location also in the perturbed portion of the flow. The steady boundary layer disturbance fields are computed as $\bar{U}_d(y, z) = \bar{U}(y, z) - \bar{U}_b(y)$ and allow for the characterization of the high-speed and low-speed regions developing in the flow, as well as for the investigation of their downstream evolution.

Additionally, HWA time-dependent velocity signal is considered to investigate the unsteady disturbances. The velocity fluctuation fields (U') allow for the identification of the highest fluctuation regions. The frequency spectra extracted at the corresponding locations outline the frequencies pertaining to the dominant fluctuation and their harmonics. Furthermore, the energy associated with the considered frequency range is computed by integrating the spectral power in the zy planes. The main results and conclusions are presented in Sec. IV.

III. STATIONARY FLOW TOPOLOGY

A. Base flow evolution

To fully characterize the unperturbed boundary layer (i.e., base flow) development, in the present work, a numerical solution of the boundary layer equations is computed for each of the three tested Re_k . The applied procedure treats the base flow as a steady and incompressible solution of the 2.5-dimensional (i.e., spanwise invariant) boundary layer equations, based on the experimentally measured pressure distribution and free-stream flow parameters. The numerical integration of the boundary layer equations is performed using a marching procedure, which initiated at the inflow with an analytical solution of the Falkner–Skan–Cooke equations.³⁶ The laminar BL velocity profile (\bar{U}_b) is then estimated from both the numerical and experimental data at each Re_k at a fixed chord location. To facilitate direct comparison with the experimental boundary layer profiles, the numerical BL is projected to the HWA measurement system through Eq. (1). The resulting comparison is reported in Fig. 2(b), while integral boundary layer parameters are shown for the three Re_k in Fig. 2(c). The obtained \bar{U}_b velocity profiles confirm that the unperturbed (i.e., no roughness

element applied) incoming boundary layer flow is fully laminar and no significant crossflow instability is developing upstream of the roughness element.

Further base flow analysis can be performed by considering the acquired IR thermography data, allowing for preliminary characterization of the wedge evolution as shown in Fig. 3. The isolated roughness element appears as a low-temperature circle at $x_r/c = 0.15$ in the reported IR images. For all three Re_k considered, the flow past the roughness element evolves into a turbulent wedge similarly to what was observed for 2D boundary layers.³ The turbulent region is deflected inboard (i.e., toward negative Z) as evolving downstream, inducing an asymmetric flow features development typical of the 3D boundary layers configurations.^{7,24} Moreover, the wedge evolution shows a monotonic behavior as the Re_k is modified. Its origin is located further away from the element for Re_{k_3} , suggesting weaker disturbance effects are introduced in the flow.

The extraction of individual surface temperature profiles along z -parallel lines delivers a quantitative estimation of the turbulent wedge development in terms of origin, width, and opening angle. Specifically, within each extracted temperature profile, the wedge is identified as a region of temperature drop with respect to the corresponding local laminar flow temperature (T_{lam}). The latter is locally extracted as the averaged temperature value of the unperturbed flow regions and is subtracted from the temperature profile to facilitate the temperature drop identifications. Regions of flow corresponding to temperature values lower than $0.9T_{lam}$ are associated with turbulent flow. This analysis is performed between $x/c = 0.158 - 0.35$, and the resulting wedge width (W) evolution is shown in Figs. 3(b), 3(d), and 3(f). The origin of the turbulent wedge is identified as the first chord location for which W is larger than $1.5D$. This representative value is chosen in similarity to the wedge geometry analysis proposed in previous works⁵ investigating the flow field incurred by an isolated element in a 2D boundary layer. The proposed procedure is based on the symmetric flow features of the developing turbulent wedge, and as such, it would be not applicable to the present case. However, the choice of the $1.5D$ as a threshold allows for the initial development of the ensuing

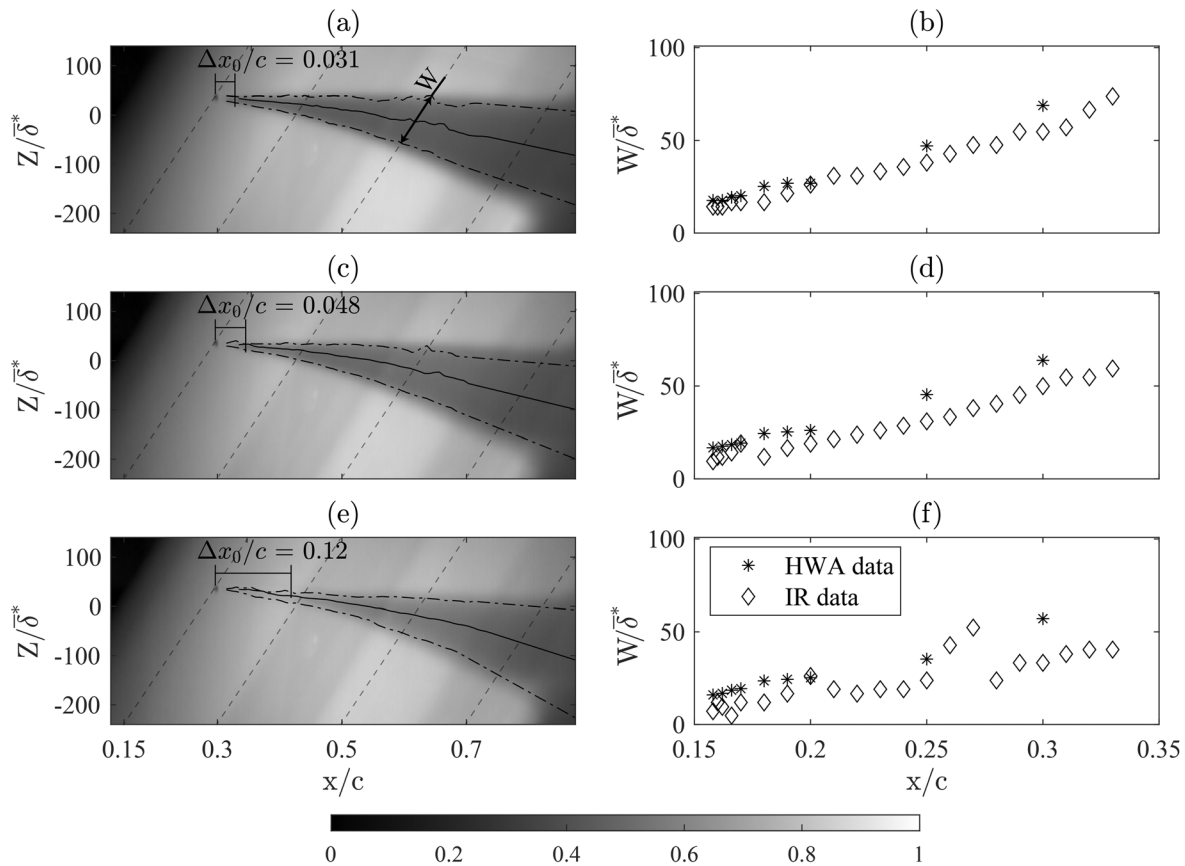


FIG. 3. (a), (c), and (e) IR thermography fields forced by roughness element at $x/c = 0.15$ and (a) $Re_{k_1} = 251$, (c) $Re_{k_2} = 222$, (e) $Re_{k_3} = 198$. Flow comes from the left, wedge middle point (- line); linear interpolation of the wedge limits (-. lines); wedge origin distance from the element ($\Delta x_0/c$). (b), (d), and (f) Estimation of wedge width (W) evolution along wing chord for different forced flow cases: element location $x/c = 0.15$ and (b) Re_{k_1} , (d) Re_{k_2} , and (f) Re_{k_3} . Values collected from post-processing of HWA (*) and IR (\diamond) data.

disturbances in the element vicinity, in agreement with the observation of a finite distance between the wedge origin and the element reported in the literature.²¹ Moreover, such a threshold is also consistent with the anticipation of unsteady disturbances and turbulent structures development due to the increase in Re_k (e.g., Refs. 1 and 21). In fact, the resulting wedge origin distance from the element location is $\Delta x_0/c = 0.03$ and 0.05 for Re_{k_1} and Re_{k_2} , respectively, while it reflects the milder disturbance effects introduced in the Re_{k_3} case, evolving for almost 12% chord before laminar breakdown occurs. These results agree well with previous works dedicated to isolated roughness elements in 2D BL flows, indicating that also in the present case the instabilities driving the transitional process are initiated in the recirculation region developing aft of the roughness element.^{5,7,21}

Overall, cases Re_{k_1} and Re_{k_2} show strong similarities, featuring wedge opening angle of approximately 8° and 9° , respectively, while Re_{k_3} features a higher opening angle of about 12° . The obtained values compare well with previous 2D boundary layer investigations.³⁵ However, for the current configurations, the traditional wedge spreading half angle definition²¹ cannot be applied since the typical symmetry of wedges in 2D boundary layers is lost. Consequently, by computing the spanwise location of the wedge center along the chord

(full black lines in Fig. 3), the angle between the wedge development axis and the X direction (hereafter called α_{skew}) is estimated, representing a measure of the overall skewness. Its values for the considered cases lay between 6° and 8° , which are angles comparable to the ones developing between the X direction and classical crossflow vortices observed in similar experimental setups, but at higher Re_{cx} numbers.^{7,30,36} The sensitivity of α_{skew} to the temperature threshold chosen for the wedge edges identification is considered as well. Few representative threshold values are selected, associating turbulent flow regions to temperature values lower than 0.85 , 0.90 , or $0.95 T_{lam}$. Absolute modifications of α_{skew} on the order of 1 to 5° (i.e., 10%–5%) are registered, respectively, for the lower and higher threshold chosen, leaving the identified α_{skew} values in a range comparable to the CFI orientation.

A comparable procedure is applied to estimate the width of the wedge from the collected HWA velocity fields. In particular, the wedge evolution can be estimated at each scanned x/c location from a spanwise velocity profile extracted at a fixed y -location close to the wall. The region of velocity drop with respect to the boundary layer velocity values at the same y is identified, giving an estimate of the wedge width also reported in Figs. 3(b), 3(d), and 3(f). Despite the different

measurement and processing techniques, the wedge evolution is comparable at all tested Re_k confirming the ability of infrared thermography to properly describe the developing changes in the boundary layer. The HWA-estimated wedge width appears to be overestimated at downstream locations (i.e., $x/c = 0.25, 0.3$), possibly due to the lower spanwise resolution when compared to the IR acquisitions. Confirming previous observations, Re_{k_3} features a wider chordwise region characterized by a slowly varying wedge width.

B. Steady disturbances

The base flow analysis corroborates that the base flow features in the present work compare well with those of previous studies (e.g., Refs. 3, 8, 22, 26, and 28). Based on these similarities, the stationary disturbances introduced by the roughness element are further analyzed, considering the HWA time-averaged velocity fields.

Figure 4 shows the disturbance velocity fields [computed as $\bar{U}(X, z) - \bar{U}_b(y/\bar{\delta}^* = 1.7)$] collected for the three Re_k at a constant $y/\bar{\delta}^* = 1.7$ distance from the wing surface. As suggested by the IR fields, an asymmetric wake is identifiable downstream of the roughness element, accompanied by the development of high- and low-speed structures, approximately aligned to the X direction. For all three cases, a low momentum region forms aft of the element,²² with a couple of alternating high- and low-speed streaks developing on both sides adjacent to the element's wake.^{12,17,18,22,26} The low momentum region persists in the wake core, up to the merging of the outer high-speed streaks. This occurs earlier for the higher Re_k considered, rapidly leading to the development of the turbulent wedge, as previously identified in the IR images (Fig. 3). The asymmetric development of the turbulent flow region is clearly evident in the largely differing behavior of the streaks located on the inboard (i.e., toward lower $Z/\bar{\delta}^*$ values) and outboard (i.e., toward higher $Z/\bar{\delta}^*$ values) sides of the wake region in the Xz plane. Specifically, the inboard high-speed streak forms shortly downstream of the element location, as shown in Fig. 4, and develops along the wake's inboard side. Once initiated, such streak structure is sustained along the downstream direction, being most likely induced by a vortex that is co-rotating with the baseflow crossflow. By contrast, the high-speed streak on the outboard side of the wake is attenuated and substituted by a large and intense low-speed streak similarly to what was described in previous works.¹⁰

These considerations are confirmed and detailed by the disturbance flow fields extracted from the HWA scans in the zy plane,

reported in Fig. 5. The low momentum region (L_1) is clearly visible in correspondence of the element's wake (L_1 , Refs. 5, 12, 22, and 45) as are the two weaker low-speed streaks developing on the element sides. The inboard low-speed region is quickly decaying and is substituted by a strong high-speed streak (H_1). The outboard low-speed streak (L_2) instead grows while moving downstream, accompanied by the dampening of the outboard high-speed structures (H_2), as observed in Fig. 4. Two high-speed regions are identified on the side of the low momentum wake region shortly downstream of the element location. They initially grow individually in the element vicinity, while they merge further downstream (forming the high-speed region named HM) replacing the low momentum region developing in the element wake, comparably to the behavior observed in 2D boundary layer configurations.²⁰

To further characterize the dominant stationary structures and their corresponding amplitudes, the disturbance velocity fields are masked based on a threshold disturbance value. This allows for isolating the two dominant low-speed regions (L_1 and L_2) and two high-speed regions (H_1 and H_2) developing downstream of the element (Fig. 5). The local absolute amplitude is estimated as the maximum and minimum disturbance velocity within the high-speed and low-speed masked regions, respectively (Fig. 6), and reflects the flow features described beforehand. The amplitude of the low-speed regions in the wake and on the inboard side of the element rapidly drops to 0, while the high-speed structures' amplitude grows prior to their merging. Further downstream, the merged high-speed region grows up to a saturation amplitude level indicative of turbulence onset.^{12,15,18,20,26}

In addition to localized absolute amplitude estimations, Andersson *et al.*² proposed a relative streak amplitude metric, that is, $A_{And}(x) = 0.5 * [\max(\bar{U} - \bar{U}_b) - \min(\bar{U} - \bar{U}_b)]$. Based on this criterion, for the present investigation, the maximum disturbance amplitude in the element vicinity is estimated to be $0.29 \bar{U}_\infty$, $0.28 \bar{U}_\infty$, and $0.25 \bar{U}_\infty$, respectively, for decaying Re_k . For 2D boundary layers, a critical streak amplitude of $0.2 \bar{U}_\infty$ is identified as a sufficient condition for the laminar breakdown of the developing velocity streaks. Hence, the streak amplitude values resulting from the present study indicate a similar transitional process is dominating the considered 3D setup. This indicates that the isolated element is introducing flow perturbations that rapidly develop in the element's wake and initiate a transitional process guided by the breakdown of the high-/low-speed streak structures. However, based on the observations reported so far

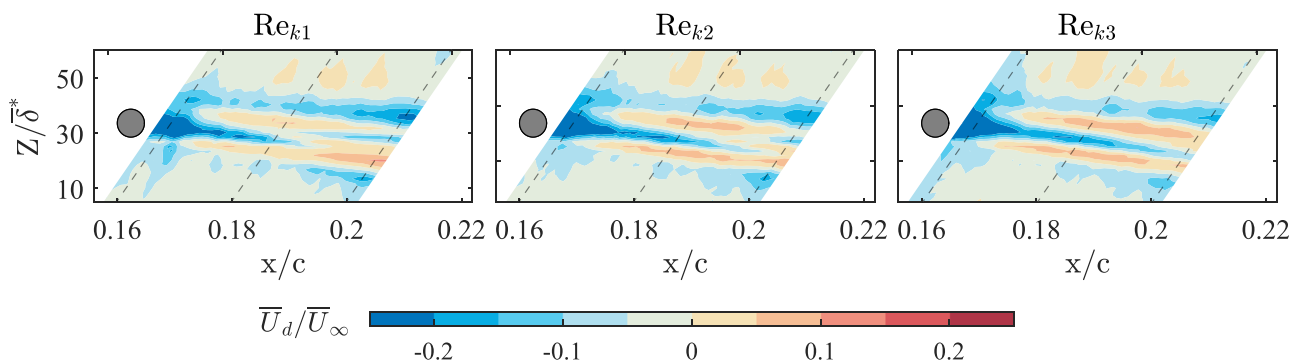


FIG. 4. Time-averaged HWA disturbance velocity fields acquired at constant wall-normal distance $y/\bar{\delta}^* = 1.7$ for $Re_{k_1} = 251$, $Re_{k_2} = 222$, and $Re_{k_3} = 198$.

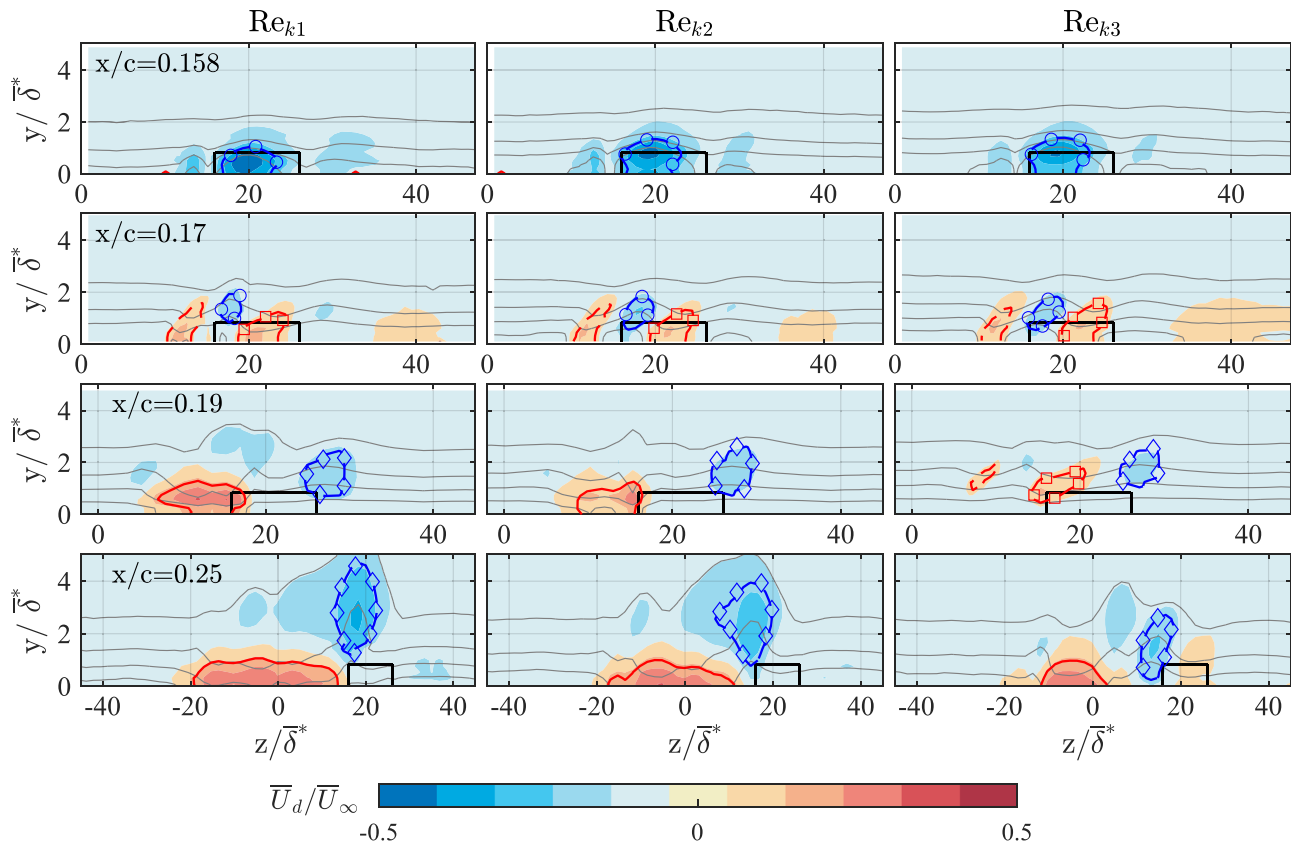


FIG. 5. Time-averaged disturbance velocity fields computed from HWA for the three Re_k at different x/c locations. Low-speed region in the elements' wake (L_1 , \circ), outboard low-speed region (L_2 , \diamond), inboard high-speed region (H_1 , - - line), outboard high-speed region (H_2 , \square), and merged high-speed region (HM , full red line). Velocity isolines plotted every 20% of the freestream speed (gray lines) and element location (black rectangle).

in this work, classical crossflow instabilities are largely absent, as the element wake is dominated by the developing system of low- and high-speed streaks. The role of baseflow crossflow appears limited to the introduction of asymmetry observed in the topology of the turbulent wedge.

IV. UNSTEADY PERTURBATIONS CHARACTERISTICS

Despite giving relevant insights on the dominant flow structures developing in the downstream vicinity of the element, the stationary disturbance analysis does not fully characterize the transitional

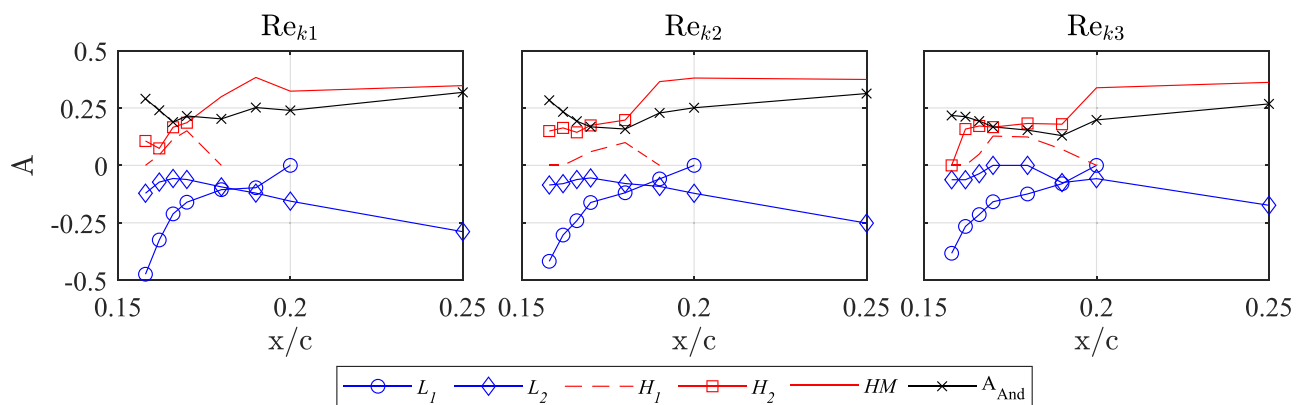


FIG. 6. Amplitude estimation of near-element flow structures for $Re_{k_1} = 251$, $Re_{k_2} = 222$, and $Re_{k_3} = 198$. Colors and symbols are identifying structures as in Fig. 5, A_{And}^2 amplitude definition (X).

process. To identify the path toward turbulence onset and to further clarify the nature of the developing instabilities, the unsteady disturbance fields are considered hereafter.

Andersson *et al.*² identify two main types of unsteady structures supported by the developing stationary streaks in the downstream vicinity of an isolated roughness element in 2D flow. Based on the aforementioned relative amplitude metric (A_{Am}), they determine streak amplitudes higher than $0.26 \bar{U}_\infty$ as sufficient to develop streak breakdown due to so-called sinuous modes associated with the stationary spanwise shear in the element wake. Instead, for a streak amplitude larger than $0.37 \bar{U}_\infty$, the varicose mode resulting from a three-dimensional shear layer instability is dominating the disturbance field. Instabilities dominated by varicose symmetry are found to be amplified in the wake flow of roughness elements in many 2D configurations, even when, according to linear stability theory, the dominant flow instability mode is of sinuous nature.^{8,9} However, the roughness configurations considered by Bucci *et al.*,^{8,9} all feature a shear ratio of approximately 1.5–2, which is much higher than the cases presented in this work (i.e., 0.85–0.9). The single-point HWA measurements performed in the current investigation prevent the extraction of information regarding the relative phase of developing unsteady disturbances. As a consequence, the collected set of data cannot provide a conclusive characterization of the nature of the vortex shedding occurring aft of the roughness element. Nonetheless, based on the works discussed beforehand by Andersson *et al.*, Bucci *et al.*, Loiseau *et al.*, and considering the streak amplitude thresholds,² the element aspect ratio ($k/D \simeq 0.08$)²⁶ and the element shear ratio ($k/\delta^* \simeq 0.85\text{--}0.9$)⁹ of the current setup, sinuous type of instabilities could dominate the shedding in the element's wake. Nevertheless, the aforementioned works are DNS computations performed on Blasius boundary layers; hence, they do not take into account the combined effect of the wing sweep angle and the chordwise variation of the pressure gradient, both affecting the local boundary layer flow stability, possibly modifying the nature and growth process of the developing instabilities. In the following section, an examination of the stationary velocity gradients and related shear layers is provided, to incur a more reliable estimation of the developing instabilities' nature.

A. Unsteady perturbation fields

To localize the flow field regions characterized by high fluctuations, the standard deviation of the point-wise time-dependent

hot-wire velocity signal (U') is considered. The U' fields computed from the HWA measurements in the Xz plane are reported in Fig. 7. For all three Re_k cases, the velocity fluctuations are concentrated in the flow region corresponding to the element's direct wake and to the later development of turbulent flow, in agreement with the orientation and configuration of the steady flow structures previously observed (Fig. 4). Similar to what was reported by previous works (e.g., Refs. 5, 22, and 26), the areas of higher fluctuations develop in correspondence to the low-speed streaks, hosting the turbulent portion of the flow. Moving downstream, the opening of the wedge region is accompanied by a corresponding spatial (spanwise) spreading and an overall increased level of unsteady fluctuations. This effect is less visible in the Re_{k_3} case, for which the developing instabilities are relatively weaker and the laminar breakdown occurs at more downstream chordwise locations.

Comparable flow features can be identified in the zy planes reported in Fig. 8 for the near-wake flow and Fig. 9 further downstream. From the near-wake flow fields, a region of intense velocity fluctuations on top of the element can be recognized. In previous investigations,^{1,7,21} this flow region is identified as responsible for the origin of the cylinder eddy shedding, which induces an increased level of unsteadiness in correspondence to the element's wake. A region of weaker unsteadiness is located on the inboard side of the roughness element, while almost no significant fluctuations are present in the rest of the flow field. As evolving downstream, the unsteady region located on top of the element expands on its flanks, possibly guided by the horseshoe vortex legs development.^{3,26} On the other hand, the fluctuation region located on the inboard element side rapidly decays. Further downstream, for the Re_{k_1} and Re_{k_2} cases, the stationary high- and low-speed streak alternation develops and the unsteady core broadens and covers a wider portion of the BL both in the z and y directions. The Re_{k_3} case is characterized by comparable flow evolution, even if the overall fluctuations are weaker and the broadening due to turbulence onset is visible at relatively more downstream chord locations.

Similar to previous analysis,¹⁶ the wall-normal and spanwise gradients of the stationary velocity field are investigated, providing interesting insights regarding the nature of the dominating unsteady instability. For the considered configuration, the wall-normal mean velocity gradients (acting on the local boundary layer velocity profile

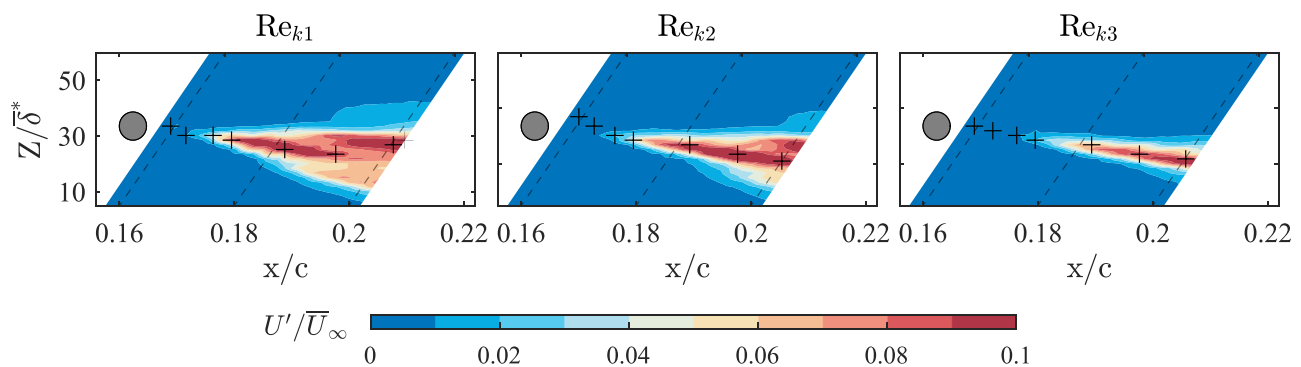


FIG. 7. Standard deviation of the HWA velocity signal acquired at constant wall-normal distance $y/\delta^* \simeq 1.7$ for $Re_{k_1} = 251$, $Re_{k_2} = 222$, and $Re_{k_3} = 198$. Points of highest std (+) computed at the same chord location of the acquired zy planes. The gray circle represents the top view of the element.

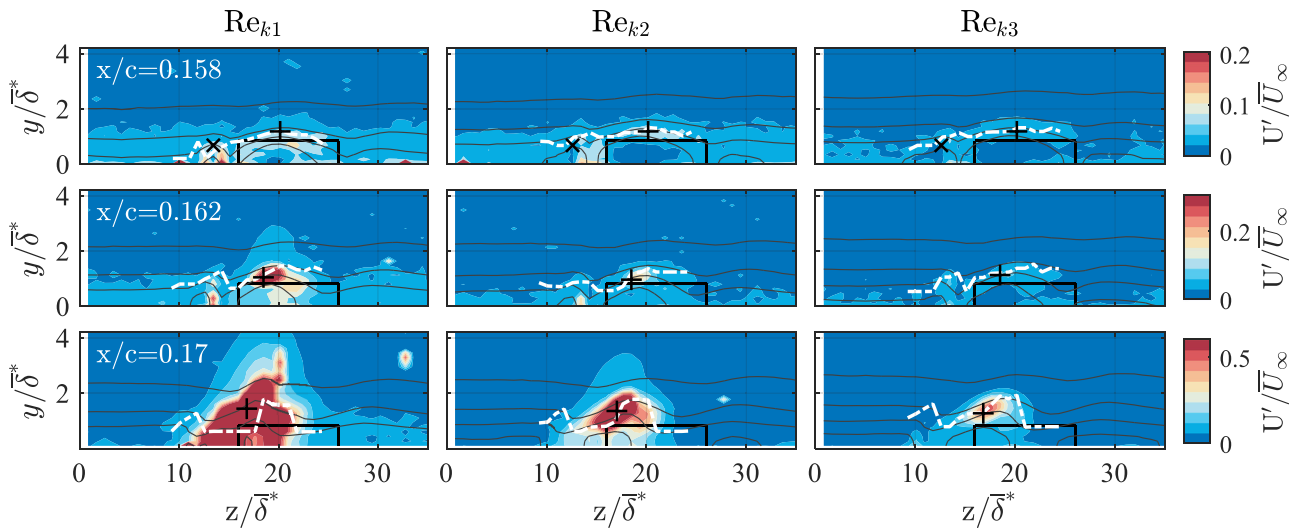


FIG. 8. Standard deviation of the HWA velocity signal at different x/c location and Re_k . Velocity isolines plotted every 20% of the freestream speed (full lines); mean velocity wall-normal gradient maximum (i.e., inflection point) (white—dotted line); maximum fluctuation amplitude location on top of the element at which spectra (Fig. 11) are extracted (+); maximum fluctuation amplitude location on the side of the element (X) at $x/c = 0.158$.

and on the small length scale of the element height) are considered to have a stronger effect on the flow with respect to their spanwise counterparts (acting on a larger length scale associated with the wedge width). Therefore, the wall-normal gradient $\partial\bar{U}/\partial y$ is first considered and computed at each spanwise location.

An inflection point in the boundary layer velocity profile is a typical source of inviscid instabilities. Inflection points are weakly identifiable on the \bar{U} profiles; however, they correspond to a local maximum or minimum of the wall-normal gradient of the mean velocity profile, as well as to a null value of the mean velocity profile

secondary derivative in y . Therefore, Figs. 10(a)–10(c) report the \bar{U} , $\partial\bar{U}/\partial y$, and $\partial^2\bar{U}/\partial y^2$ profiles for the three Re_k cases extracted at a fixed chord location of $x/c = 0.162$ and a spanwise position located inside the wake of the element (i.e., $z/\delta^* = 19.5$). The corresponding profiles of the standard deviation of velocity fluctuations are also reported in these graphs and multiplied by a factor of 10 to ease visualization. It is evident that for the considered chord location, the $\partial\bar{U}/\partial y$ maximum coincides with the U' maximum. Accordingly, the same y -location corresponds to the null value of the secondary derivative profile, that is, $\partial^2\bar{U}/\partial y^2$, thus identifying

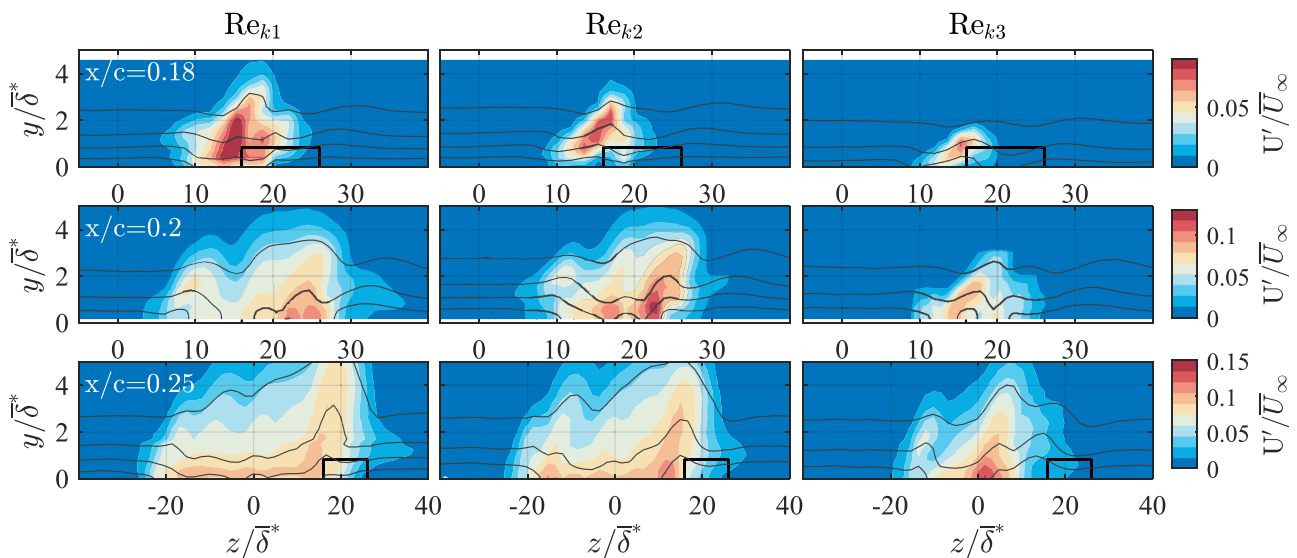


FIG. 9. Standard deviation of the HWA velocity signal at different x/c location and Re_k . Velocity isolines plotted every 20% of the freestream speed (full lines).

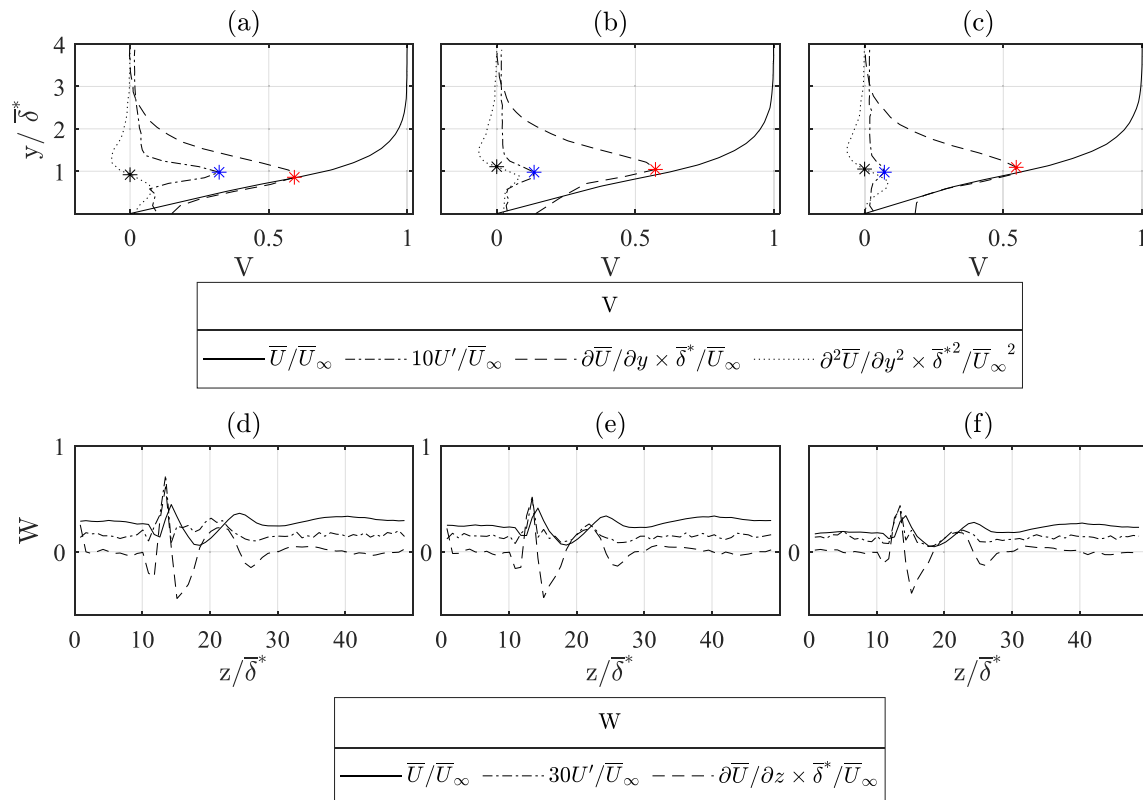


FIG. 10. (a)–(c) Time-averaged velocity profile, $\partial\bar{U}/\partial y$ gradient profile, $\partial^2\bar{U}/\partial y^2$ profile, and fluctuation amplitude profile extracted at $z/\delta^* = 19.5$, $x/c = 0.162$ for (a) $Re_{k_1} = 251$, (b) $Re_{k_2} = 222$, and (c) $Re_{k_3} = 198$. Maximum of $\partial\bar{U}/\partial y$ gradient profile (red *) and maximum of fluctuation amplitude profile (blue *); inflection point of $\partial^2\bar{U}/\partial y^2$ profile (black *). (d)–(f) Time-averaged velocity profile, $\partial\bar{U}/\partial z$ gradient profile, and standard deviation profile extracted at $y/\delta^* \simeq 1$, $x/c = 0.162$ for (d) $Re_{k_1} = 251$, (e) $Re_{k_2} = 222$, and (f) $Re_{k_3} = 198$.

an inflection point of the \bar{U} profiles. Similar behavior is observed at most spanwise locations where inflectional points appear within the wake. Such inflection points are not directly visible in the boundary layer profiles reported in Fig. 10; however, their wall-normal location is shown by the white dashed line reported in the contours of Fig. 8. The observed correspondence suggests that the development of the dominant instabilities strongly relates to the wall-normal shear layer evolution.¹⁶ The extracted fluctuation spectra at these locations (Fig. 11) further confirm this connection, showing the presence of a main high-amplitude peak and increasingly amplified harmonics as Re_k is increased. Hence, the inflectional boundary layer profile inherently contributes to the instabilities sustainment and growth process; however, in the considered near-critical amplitude range, a different mechanism is responsible for initiating the unsteady disturbances (as further discussed in Sec. IV B). The correspondence between the fluctuation amplitude local maxima and the gradient maxima is lost at more downstream locations as the flow becomes turbulent. This is already visible at $x/c = 0.17$ for case Re_{k_1} (Fig. 8); therefore, the maximum gradient location is not reported in the flow fields of Fig. 9 for the sake of clarity.

A similar analysis can be performed for the spanwise gradients of the mean velocity field. The standard deviation fields, along with the already discussed $\partial\bar{U}/\partial y$, show that the region of higher fluctuations

lies at a wall-normal location of $y/\delta^* \simeq 1$ in the element vicinity. Therefore, to visualize the $\partial\bar{U}/\partial z$ gradient profile, the spanwise mean velocity and fluctuation standard deviation profiles are extracted at the same y -location. The $\partial\bar{U}/\partial z$ is then computed for these velocity profiles. The results are reported in Figs. 10(d)–10(f) for $x/c = 0.162$ at all three Re_k numbers measured. The spanwise gradient behavior confirms that the low-speed streaks are the regions containing higher unsteady fluctuations. As stated previously and in agreement with previous works (e.g., Refs. 5, 22, and 26), the minimum of the velocity appears to be aligned with the maximum of the fluctuation amplitude.

Considering the reported results, the developing instabilities strongly relate to the region of inflectional velocity fields in the element’s wake and the related shear layers, similar to the results of numerical and experimental investigations dedicated to isolated roughness elements in 2D BL. This behavior suggests that, in analogy with the 2D cases, shedding phenomena near the element play a dominant role. Additional information to further ascertain these dominant instabilities’ nature can be inferred by analyzing the features of the frequency spectra extracted from the time-resolved velocity signals. Further confirming the observations from the analysis of the stationary disturbance fields, locally generated crossflow instabilities do not appear to manifest or influence the near-element flow development.^{7,24}

B. Spectral and intermittency analysis

The time-dependent velocity signal is analyzed to extract the frequency spectra in correspondence to the maximum velocity fluctuation loci, which indicated with the black cross in Fig. 8. The velocity signal power spectral density (PSD) is computed through a Welch⁴² periodogram procedure implemented in MATLAB, resulting in a final frequency resolution of 25 Hz. The extracted spectra are collected in Fig. 11 and clearly show the higher amplitude of fluctuations present in the element wake with respect to the freestream flow regions (gray lines in the plots).^{5,23} The near-wake flow is characterized by a strongly tonal behavior, with PSD peaks identifying dominant frequencies in the 1.4–1.9 kHz bandwidth. Specifically, the peak frequency (f_1) monotonically decreases with Re_k , corresponding to 1.85, 1.65, and 1.45 kHz for the three Re_k cases. Moreover, harmonics of f_1 are also well defined between $x/c = 0.162$ and $x/c = 0.17$ for Re_{k_1} and Re_{k_2} , while they persist even more downstream for Re_{k_3} . At more downstream locations ($x/c > 0.17$), the spectra are characterized by overall higher fluctuations level, which is spread over a broader frequency range without identifying a clear spectral peak. This behavior is indicative of the

laminar structure breakdown and is observed with a 3% chord delay for Re_{k_3} , in agreement with the results discussed beforehand and confirming that the instabilities developing in this lower Re_k case are milder. The observed spectral behavior bears strong similarity to 2D boundary layer transition cases, thus indicating that the crossflow velocity component has limited effect on the unsteady disturbance onset. This agrees well with the comparable 2D and 3D boundary layer flow topology observed by Kurz and Kloker,²⁴ and is first confirmed experimentally by the presented investigation.

In particular, the comparability between the two boundary layer scenarios lends some useful observations for the present cases. In a typical 2D boundary layer configuration, the tonal behavior observed in the element vicinity can either be driven by the amplification of a local instability mode,⁸ or by the quasi-resonance of a marginally stable mode, originating from background noise or external disturbances and enhanced by the roughness element.⁹ Past investigations highlighted that the occurring behavior is strongly related to multiple geometrical and freestream parameters, in which Re_k , k/D , k/δ^* , and T_u .⁸ In 3D boundary layers, the pressure gradient and sweep angle

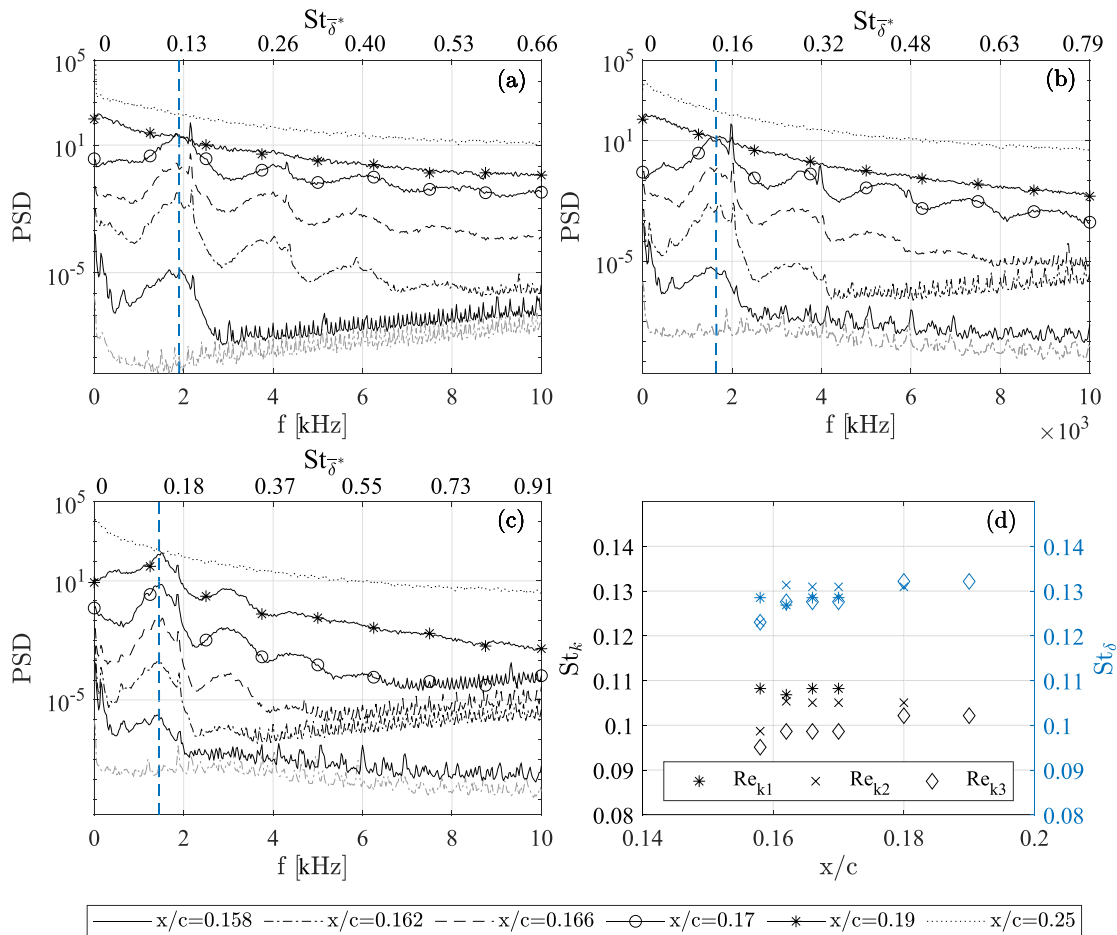


FIG. 11. (a)–(c) Frequency spectra extracted for different Re_k in correspondence to the maximum fluctuation amplitude region for each chord location acquired. For visualization purposes, the spectra pertaining to each chord location are offset by a decade. Freestream flow frequency spectra extracted at $x/c = 0.158$ (gray horizontal line); spectral peak (blue dotted line). (a) $Re_{k_1} = 251$, (b) $Re_{k_2} = 222$, (c) $Re_{k_3} = 198$. (d) St_k and St_{δ^*} extracted for different Re_k and chord locations at the location of maximum std.

may also play an additional and relevant role, as they significantly affect the local boundary layer stability and evolution. In the current work, a direct comparison between the experimentally identified dominant instabilities and the dominant modes identified by a numerical stability solution is not available. Therefore, it is not possible to provide conclusive proof regarding the nature of the roughness element behavior. Nonetheless, the extremely low level of freestream turbulence characterizing the wind tunnel flow in the present investigation ($T_u = 0.025 \bar{U}_\infty$,³⁶ much lower than that considered in 2D investigations⁸) tends to limit the role of the resonating behavior of the roughness element. This, in turn, would point toward the amplification of instability modes as the main mechanism responsible for the unsteadiness development. Such behavior would agree with the fact that the transitional flow scenario of the current setup is dominated by the rapid amplification of convective instabilities, which are typically enhanced by the roughness element.²⁸ Additionally, as visible from the spectra reported in Fig. 11, the dominant frequency peak is relatively broad. Accordingly, in the element vicinity, a small range of frequencies can be excited, inducing a range of instability modes initially growing due to non-modal interactions and transient phenomena.^{8,40,41,44} Further sustaining this hypothesis, recent investigations⁴⁶ showed that transient phenomena can be relevant in the initial phases of the receptivity process of a roughness element applied in a 3D boundary layer. These observations do not exclude the possibility of exciting weaker modes by means of the roughness resonant behavior; nonetheless, this mechanism would play a less relevant role in the transitional process.

Toward confirming that the identified tonal behavior can be associated with the amplification of boundary layer instabilities, the extracted dominant frequencies are compared to those pertaining to the element shedding,^{21,22} by estimating the local Strouhal number. For this analysis, the Strouhal number is defined as $St_{\delta^*} = f_1 \times \delta^* / |\mathbf{u}_k|$, or as $St_k = f_1 \times k / |\mathbf{u}_k|$, where k is the element height and $|\mathbf{u}_k|$ is the unperturbed boundary layer velocity at height k extracted from the BL numerical solution for the three considered Re_k .^{1,12,21} The former definition (St_{δ^*}) proved helpful in comparing the spectral characteristics within a universal frame,²¹ while the St_k is strongly dependent on the Re_k as it also accounts for the local boundary layer development and its relation to the element geometry. Both St number definitions are based on the reference frequency corresponding to the maximum of the PSD spectra at each chord location considered and are collected in

Fig. 11. The tonal behavior outlined by the reported spectra reflects in the St_{δ^*} values, which retain an almost constant value in the range of 0.12–0.13 throughout all the cases considered. On the other hand, the St_k values are weakly scaling with the Re_k . A direct comparison between the St numbers extracted in the present work with cases presented in literature is difficult to achieve, as due to the 3D nature of the considered boundary layer, the Re_k and k/D considered herein lay outside of the typical parameter range explored in 2D boundary layer investigations.^{12,21,22} Nonetheless, in the element vicinity, the St_k values fall within the range of values generally associated with cylinder shedding,^{21,22} namely, $St_k \simeq 0.09$ – 0.12 . This further suggests that the instability onset process is initiated and dominated by the element shedding. Nonetheless, the St number definition loses its relevance once turbulence begins to play an important role in the BL, as the tonal behavior and shedding are overcome by the increased level of broadband fluctuations. As such, St values are only reported for the chord locations characterized by spectra with a clearly identified frequency peak (i.e., upstream of $x/c = 0.2$).

The performed Welch’s periodogram analysis additionally provides the spectral power of the acquired point-wise velocity signal. Hence, the spectral power values corresponding to each frequency can be integrated into the zy plane to obtain an estimate of the associated integral energy (hereafter named E_{PS} and non-dimensionalized by \bar{U}_∞^2) and its location in the frequency space. The contours of the resulting integrated energy are reported in Fig. 12, using a logarithmic color scale for visualization purposes. The strong tonal behavior is confirmed for all three Re_k in the element vicinity. In particular, local energy peaks corresponding to the dominant frequency and its harmonics can be identified. The chordwise instability growth is initially accompanied by an energy growth of the sole dominant frequencies, while a global energy increase spread over the whole considered frequency bandwidth occurs with the turbulence onset. The spreading of spectral energy occurs more downstream for the lower Re_k cases, in agreement with the results previously reported.

Finally, the velocity signal intermittency (γ) is estimated.^{22,31} The resulting contours are reported in Fig. 13 for a set of chord locations between $x/c = 0.17$ – 0.25 . More upstream chord locations are not reported as they show no or little relevant region of intermittency; that is, γ is approximately zero in the whole domain. Nonetheless, the well-developed $\gamma \simeq 1$ regions characterizing the Re_{k1} case are indicative of the early development of the turbulent wedge observed for this

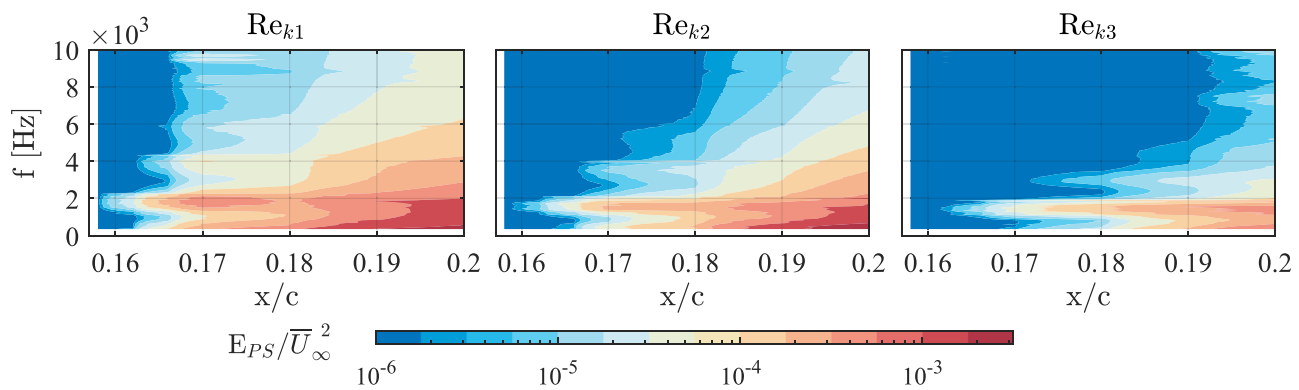


FIG. 12. Contour plots of integral energy ($E_{PS} \bar{U}_\infty^2$) extracted from the integration of the spectral power computed through the Welch periodogram.

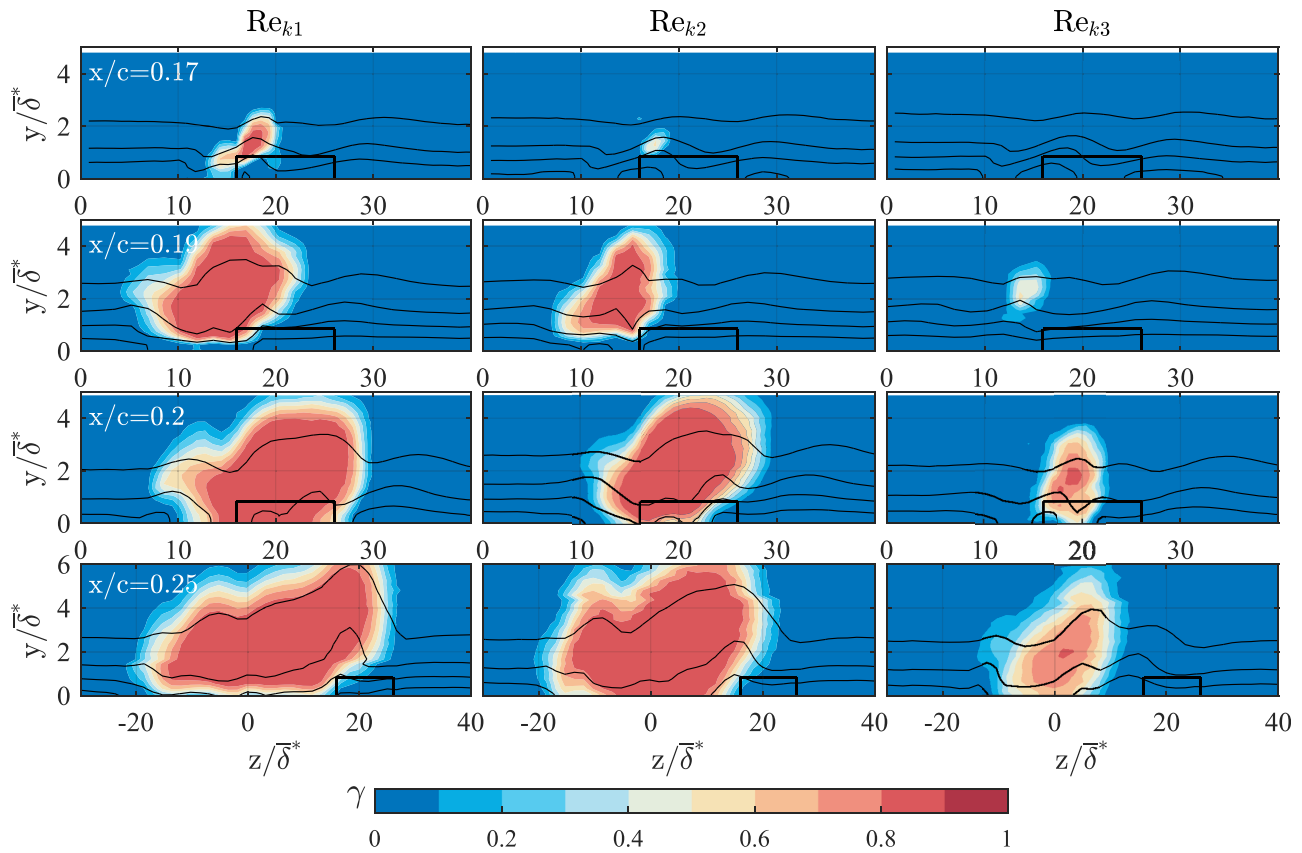


FIG. 13. Intermittency contours estimated for three different Re_k at the indicated chord locations.

super-critical case. The Re_{k_2} case closely follows this behavior, displaying a highly turbulent region quickly extending in both the spanwise and wall-normal directions as moving downstream. Minor turbulence spreading is observed for the Re_{k_3} case, in agreement with all other observations reported for this case. The analysis of the intermittency highlights the asymmetric development of the turbulent flow region. Especially considering the Re_{k_3} case, thanks to the slower turbulence spreading, the turbulent structure is observed to shift toward negative z coordinates while moving downstream, in agreement with the asymmetrical wedge opening observed in Fig. 3. Moreover, it is also possible to identify the overhang effect of the turbulent region; that is, the sides of the $\gamma > 0$ region always appear to be separated from the wall by a thin laminar layer. Overall, the γ evolution confirms how the higher fluctuation region is initially located in the element wake, while all three Re_k show a turbulent region spreading in the spanwise and wall normal directions at $x/c = 0.25$, with high γ values characterizing a wider portion of the domain.

In conclusion, the collected results indicate that the developing near-element instabilities are strongly related to the wall-normal shear layer evolution, and are effectively sustained by the inflectional nature of the boundary layer velocity profile. In fact, the analysis of the standard deviation and gradient peaks allows for the identification of an inflection point that coincides with the y -location of maximum fluctuations developing on top of the element. Based also on the observed

dominant frequency, the developing instabilities are initiated by the shedding process occurring on the element top. The introduced instabilities persist and grow in the element's wake, influencing a wider region of the acquired domain and leading to the formation of a turbulent wedge. Overall, the near-element flow development and the instability onset process are considered to be qualitatively comparable to the one observed in 2D boundary layer studies, confirming that classical modal crossflow instabilities are not dominating the present transitional scenario. Nonetheless, the presence of the crossflow velocity component in the boundary layer baseflow fundamentally conditions the downstream flow development in the 3D boundary layer scenario, introducing a flow asymmetry affecting the evolution of both steady and unsteady flow features.

V. CONCLUSIONS

The present study investigates the transitional process of a 3D boundary layer forced by an isolated cylindrical roughness element applied on the surface of a swept wing model. By varying the free-stream velocity, the flow is investigated at super-critical (i.e., Re_{k_1} , causing flow tripping aft of the element location) and two critical (i.e., Re_{k_2} , Re_{k_3}) conditions through infrared thermography and hot-wire anemometry. Detailed geometrical parameters of the measured configurations are reported in Table II.

The current setup develops a base flow topology comparable to the dominant flow features identified in 2D boundary layers, suggesting that roughness-induced crossflow instabilities are not dominant in the considered 3D boundary layer. This can be traced back to the relatively high amplitude of the applied isolated element, which introduces steady and unsteady disturbances that rapidly develop and cause flow tripping. Nonetheless, notable differences between isolated roughness transition in 2D and 3D boundary layers are identified. These mostly derive from the presence of the crossflow velocity component in the boundary layer base flow, which induces asymmetric downstream development of the identified near-element flow features.

Specifically, the turbulent flow region forms at a finite distance from the element location (i.e., $\Delta x_0/c = 0.03\text{--}0.12$ for decreasing Re_k)²¹ and evolves following an inboard-tilted trajectory. This is described by the parameter α_{skew} , which is found to correspond to the trajectory of classical modal crossflow vortices developing in the same geometry at higher Re (i.e., a $6^\circ\text{--}8^\circ$ angle with respect to the X direction).³⁸

Additionally, the stationary near-element flow topology features one main low-speed flow region developing aft of the element in correspondence to its wake. This is accompanied by the alternation of two high-/low-speed streaks on its inboard and outboard sides. The high-speed structures evolve individually in the element's vicinity; however, they merge further downstream and substitute the low-speed wake streak. This high-speed region localizes in correspondence to the turbulent wedge region, growing asymmetrically up to saturation.

On the other hand, the crossflow velocity component has limited effect on the unsteady instabilities onset and dominant frequencies. In fact, detailed analysis of the unsteady velocity signal suggests that the unsteady instabilities are initiated by the shedding process occurring on top of the element. This compares well with previously investigated 2D boundary layer scenarios and is first confirmed for a 3D boundary layer configuration in the present work. Additionally, the y -location of the maximum fluctuation region corresponds to the wall-normal gradient maximum, indicating that the inflectional boundary layer profile inherently contributes to the unsteady instabilities sustainment and growth process. Furthermore, the spectral analysis of the time-dependent velocity signal shows a tonal behavior dominating the near-element flow development (upstream of the onset of turbulence), with dominant frequency monotonically varying with Re_k . The definition of the Strouhal number based on the identified frequency peak provides values that lay within the shedding range identified in the literature (namely, $St_{\xi^*} \simeq 0.12\text{--}0.13$ and $St_k \simeq 0.09\text{--}0.12$).^{1,12,21} However, despite the similarities observed in the near-element flow region, the baseflow crossflow component actively conditions the instabilities downstream development and the entire transition topology. This is confirmed by the asymmetric spanwise and wall-normal broadening of the high-fluctuations region and of the area of elevated intermittency (representative for the turbulent flow region).

ACKNOWLEDGMENTS

The authors are grateful to the European Research Council for financially supporting this research through the GLOWING Starting Grant (Grant No. 803082). A dedicated acknowledgement goes to S. Bernardy and E. Langedijk for sharing their technical knowledge during the experimental preparation. The authors would

also like to thank their direct colleagues for their contribution and support during this investigation and the anonymous referees for their helpful suggestions.

AUTHOR DECLARATIONS

Conflict of Interest

The authors have no conflicts to disclose.

Author Contributions

Giulia Zoppini: Conceptualization (equal); Data curation (equal); Formal analysis (equal); Investigation (equal); Methodology (equal); Software (equal); Validation (equal); Visualization (equal); Writing – original draft (equal); Writing – review and editing (equal). **Daniele Ragni:** Conceptualization (equal); Supervision (equal); Visualization (equal); Writing – review and editing (equal). **Marios Kotsonis:** Conceptualization (equal); Data curation (equal); Formal analysis (equal); Funding acquisition (equal); Investigation (equal); Methodology (equal); Project administration (equal); Resources (equal); Supervision (equal); Validation (equal); Visualization (equal); Writing – review and editing (equal).

DATA AVAILABILITY

The data that support the findings of this study are available from the corresponding author upon reasonable request.

REFERENCES

- ¹M. Acarlar and C. Smith, "A study of hairpin vortices in a laminar boundary layer. Part 1. Hairpin vortices generated by a hemisphere protuberance," *J. Fluid Mech.* **175**, 1–41 (1987).
- ²P. Andersson, L. Brandt, A. Bottaro, and D. Henningson, "On the breakdown of boundary layer streaks," *J. Fluid Mech.* **428**, 29–60 (2001).
- ³C. Baker, "The laminar horseshoe vortex," *J. Fluid Mech.* **95**, 347–367 (1979).
- ⁴A. R. Berger, M. N. McMillan, E. B. White, S. Suryanarayanan, and D. B. Goldstein, "Suppression of transition behind a discrete roughness element using a downstream element," in *Tenth International Symposium on Turbulence and Shear Flow Phenomena* (Begel House Inc., 2017).
- ⁵A. R. Berger and E. B. White, "Experimental study of the role of high- and low-speed streaks in turbulent wedge spreading," AIAA Paper No. AIAA 2020-0832, 2020.
- ⁶H. Bippes, "Basic experiments on transition in three-dimensional boundary layers dominated by crossflow instability," *Prog. Aerosp. Sci.* **35**(4), 363–412 (1999).
- ⁷M. Brynjell-Rahkola, P. Schlatter, A. Hanifi, and D. Henningson, "Global stability analysis of a roughness wake in a Falkner-Skan-Cooke boundary layer," *Procedia IUTAM* **14**, 192–200 (2015).
- ⁸M. A. Bucci, S. Cherubini, J. C. Loiseau, and J. C. Robinet, "Influence of free-stream turbulence on the flow over a wall roughness," *Phys. Rev. Fluids* **6**, 063903 (2021).
- ⁹M. A. Bucci, D. K. Puckert, C. Andriano, J. C. Loiseau, S. Cherubini, J. C. Robinet, and U. Rist, "Roughness-induced transition by quasi-resonance of a varicose global mode," *J. Fluid Mech.* **836**, 167–191 (2018).
- ¹⁰V. G. Chernoray, A. V. Dovgal, V. V. Kozlov, and L. Loeffdahl, "Experiments on secondary instability of streamwise vortices in a swept-wing boundary layer," *J. Fluid Mech.* **534**, 295 (2005).
- ¹¹S. Cherubini, M. de Tullio, P. de Palma, and G. Pascazio, "Transient growth in the flow past a three-dimensional smooth roughness element," *J. Fluid Mech.* **724**, 642–670 (2013).
- ¹²M. Choudhari and P. Fischer, "Roughness-induced transient growth," in *35th AIAA Fluid Dynamics Conference and Exhibit* (American Institute of Aeronautics and Astronautics, 2005).

- ¹³J. Chu and D. Goldstein, "Investigation of turbulent wedge spreading mechanism with comparison to turbulent spots," AIAA Paper No. AIAA 2012-751, 2012.
- ¹⁴J. Dagenhart and W. S. Saric, "Crossflow stability and transition experiments in swept-wing flow," Report No. NASA/TP-1999-209344 (NASA, 1999).
- ¹⁵N. A. Denissen and E. B. White, "Secondary instability of roughness-induced transient growth," *Phys. Fluids* **25**, 114108 (2013).
- ¹⁶F. Ergin and E. White, "Unsteady and transitional flows behind roughness elements," *AIAA J.* **44**, 2504–2514 (2006).
- ¹⁷J. Fransson, L. Brandt, A. Talamelli, and C. Cossu, "Experimental study of the stabilization of Tollmien–Schlichting waves by finite amplitude streaks," *Phys. Fluids* **17**, 054110 (2005).
- ¹⁸J. H. M. Fransson, L. Brandt, A. Talamelli, and C. Cossu, "Experimental and theoretical investigation of the nonmodal growth of steady streaks in a flat plate boundary layer," *Phys. Fluids* **16**, 3627–3638 (2004).
- ¹⁹N. Gregory and W. Walker, *The Effect on Transition of Isolated Surface Excrescences in the Boundary Layer* (HM Stationery Office, 1956).
- ²⁰J. Kendall, "Laminar boundary layer velocity distortion by surface roughness: Effect upon stability," AIAA Paper No. 195, 1981.
- ²¹P. S. Klebanoff, W. G. Cleveland, and K. D. Tidstrom, "On the evolution of a turbulent boundary layer induced by a three-dimensional roughness element," *J. Fluid Mech.* **237**, 101–187 (1992).
- ²²M. Kuester and E. White, "Structure of turbulent wedges created by isolated surface roughness," *Exp. Fluids* **57**, 47 (2016).
- ²³M. S. Kuester and E. B. White, "Roughness receptivity and shielding in a flat plate boundary layer," *J. Fluid Mech.* **777**, 430–460 (2015).
- ²⁴H. Kurz and M. Kloker, "Mechanisms of flow tripping by discrete roughness elements in a swept-wing boundary layer," *J. Fluid Mech.* **796**, 158–194 (2016).
- ²⁵M. Landahl, "A note on an algebraic instability of inviscid parallel shear flows," *J. Fluid Mech.* **98**, 243–251 (1980).
- ²⁶J. Loiseau, J. Robinet, S. Cherubini, and E. Leriche, "Investigation of the roughness-induced transition: Global stability analyses and direct numerical simulations," *J. Fluid Mech.* **760**, 175–211 (2014).
- ²⁷F. Munaro, *Mechanisms of Boundary Layer Transition Due to Isolated Roughness on Swept wings: An Experimental Study* (TU Delft Aerospace Engineering, 2017).
- ²⁸D. K. Puckert and U. Rist, "Experiments on critical Reynolds number and global instability in roughness-induced laminar–turbulent transition," *J. Fluid Mech.* **844**, 878–904 (2018).
- ²⁹D. K. Puckert and U. Rist, "Experimental observation of frequency lock-in of roughness-induced instabilities in a laminar boundary layer," *J. Fluid Mech.* **870**, 680–697 (2019).
- ³⁰R. Radeztsky, M. Reibert, and W. Saric, "Effect of isolated micron-sized roughness on transition in swept-wing flows," *AIAA J.* **37**, 1370–1377 (1999).
- ³¹O. N. Ramesh, J. Dey, and A. Prabhu, "Transitional intermittency distribution in a three-dimensional constant pressure diverging flow," *Exp. Fluids* **21**, 259–263 (1996).
- ³²M. Reibert, W. Saric, J. Carrillo, and K. Chapman, "Experiments in nonlinear saturation of stationary crossflow vortices in a swept-wing boundary layer," AIAA Paper No. 96-0184, 1996.
- ³³A. Rius-Vidales, M. Kotsonis, A. Antunes, and R. Cosin, "Effect of two-dimensional surface irregularities on swept wing transition: Forward facing steps," AIAA Paper No. AIAA 2018-3075, 2018.
- ³⁴W. Saric, H. Reed, and E. White, "Stability and transition of three dimensional boundary layers," *Annu. Rev. Fluid Mech.* **35**, 413–440 (2003).
- ³⁵G. B. Schubauer and P. S. Klebanoff, "Contributions to the mechanics of boundary-layer transition," Technical Report No. 3489, National Advisory Committee for Aeronautics (1955).
- ³⁶J. Serpieri, "Cross-flow instability," Ph.D. thesis (TU Delft, 2018).
- ³⁷J. Serpieri and M. Kotsonis, "Design of a swept wing wind tunnel model for study of cross-flow instability," AIAA Paper No. AIAA 2015-2576, 2015.
- ³⁸J. Serpieri and M. Kotsonis, "Three-dimensional organisation of primary and secondary crossflow instability," *J. Fluid Mech.* **799**, 200–245 (2016).
- ³⁹I. Tani, "Boundary-layer transition," *Annu. Rev. Fluid Mech.* **1**, 169–196 (1969).
- ⁴⁰D. Tempelmann, A. Hanifi, and D. Henningson, "Spatial optimal growth in three-dimensional compressible boundary layers," *J. Fluid Mech.* **704**, 251–279 (2012).
- ⁴¹D. Tempelmann, L. Schrader, A. Hanifi, L. Brandt, and D. Henningson, "Swept wing boundary-layer receptivity to localized surface roughness," *J. Fluid Mech.* **711**, 516–544 (2012).
- ⁴²P. Welch, "The use of fast Fourier transform for the estimation of power spectra: A method based on time averaging over short, modified periodograms," *IEEE Trans. Audio Electroacoust.* **15**, 70–73 (1967).
- ⁴³E. White and W. Saric, "Secondary instability of crossflow vortices," *J. Fluid Mech.* **525**, 275–308 (2005).
- ⁴⁴E. B. White, J. M. Rice, and F. Gökhan Ergin, "Receptivity of stationary transient disturbances to surface roughness," *Phys. Fluids* **17**, 064109 (2005).
- ⁴⁵Q. Ye, F. Schrijer, and F. Scarano, "Geometry effect of isolated roughness on boundary layer transition investigated by tomographic PIV," *Int. J. Heat Fluid Flow* **61**, 31–44 (2016).
- ⁴⁶G. Zoppini, S. Westerbeek, D. Ragni, and M. Kotsonis, "Receptivity of cross-flow instability to discrete roughness amplitude and location," *J. Fluid Mech.* **939**, A33 (2022).